

Fluid-structure Interaction of a Fully Passive Flapping Foil for Flow Energy Extraction

M. N. Mumtaz Qadri^{1,2,#}, F. W. Zhao^{1,#}, H. Tang^{1,*}

¹Research Center for Fluid-Structure Interactions, Department of Mechanical Engineering, The Hong Kong Polytechnic University, Kowloon, Hong Kong, China

²Department of Aerospace Engineering, College of Aeronautical Engineering, National University of Sciences and Technology, Risalpur, Pakistan

[#]These authors contributed equally to this work

^{*}Corresponding author: h.tang@polyu.edu.hk

ABSTRACT

We experimentally investigated the fluid-structure interaction (FSI) and energy extraction performance of a novel flapping-foil based flow-energy harvester. Different from most of existing concepts, this device can extract energy from flows through a foil's fully passive flapping motion, i.e., the foil's heaving and pitching motions are induced by the flow without using any actuator. The foil's dynamics and energy extraction performance were studied under various flow and operating conditions. It was found that, when operating at the Reynolds number near 10^5 , the device has a cut-in speed of $U_\infty = 0.45$ m/s and can generate a mean power of about 1 W in a water flow of $U_\infty = 0.55$ m/s, leading to a power conversion efficiency of 32.5%. Detailed FSI studies revealed that both the heaving and pitching motions can make positive contributions to energy harvesting. The heaving velocity reaches its extremes at the end of each pure heaving phase, whereas the heaving force reaches its extremes at around the end of each stroke reversal, leading a phase difference of nearly 90° . As such, the heaving power is positive in the pure heaving phases but negative in the stroke reversal phases. Both the pitching velocity and pitching moment peak at the end of stroke reversals, hence generating a significant peak in the pitching power. It was also found that, compared to the foil's effective angle of attack, the leading-edge vortices produced during flapping have a very limited impact on the foil's dynamics. A parametric study revealed that, as the foil's pivot axis is moved towards the trailing edge, both the mean heaving power and the mean pitching power increase. As a result, the total power increases significantly. The same trend was also observed when the foil's pitching amplitude increases from 30° to 60° . On the contrary, it seems that there exists an optimal water speed between 0.46 and 0.69 m/s, at which the power conversion efficiency is maximum.

1. INTRODUCTION

The ever-increasing energy demands and growing environmental concerns on fossil fuel encourage the development and implementation of technologies to extract energy from renewable resources, such as air flow, water flow and sunlight. Among various technologies, rotary turbines have been widely used in winds or tides due to their high energy conversion efficiencies. Besides this classical, mature technology, some novel technologies were also proposed, e.g. wind energy harvesting using coupled vortex induced vibration and galloping phenomena (Sun et al., 2019). Another type of concepts that extract air/water flow energy using flapping foils was also proposed, earliest by McKinney & DeLaurier (1981). Compared with conventional rotary turbines, these energy converters are centrifugal stress free and hence are structurally more robust. Also, due to the relatively low tip speeds, they are environmentally friendly, thus reducing the impact on flying/aquatic animals. Furthermore, they can be deployed in wide and shallow water flows due to their rectangular sweep area (Xiao & Zhu, 2014). Through theoretical and experimental studies, McKinney & DeLaurier (1981) found that the energy conversion efficiency of these concepts can be comparable to that of rotary turbines.

The flapping-foil based flow energy extraction has three different driving modes: the *fully active* mode where both the heaving and pitching motions are prescribed, the *semi-active* mode where one of the motions is prescribed while the other is flow induced, and the *fully passive* mode where both the motions are flow induced. Extensive studies have been carried out for harvesters operating in the fully active and semi-active modes. By imposing prescribed sinusoidal pitching and heaving motions on a NACA0015 foil in a flow at the Reynolds number 1100, Dumas & Kinsey (2006) and Kinsey & Dumas (2012) realized a maximum energy conversion efficiency of 34% when the foil is operated with the reduced frequency in the range of 0.75 ~ 1.13, the pivot axis located at 1/3 chord from the leading edge, the pitching amplitude in the range of 70° ~ 80°, the heaving amplitude of one chord and the heaving-pitch phase difference of 90°. In this optimum case, the foil's maximum heaving velocity is close to the freestream velocity, and the effective angle of attack is as high as 35°. They also observed that shedding of leading-edge vortices (LEVs) right before the completion of stroke reversal helped improve the power generation (Kinsey & Dumas, 2008). Xiao et al. (2012) numerically investigated a NACA0012 foil based fully active flow energy harvester and explored the improvement of power generation through tuning the pitch motion. It was found that under

certain conditions pitching in trapezoid profiles can convert more energy than that in sinusoidal profiles.

The semi-active mode was usually realized by prescribing the foil's pitching motion and letting the flow drive the foil's heaving motion. Shimizu et al. (2008) designed and numerically studied a NACA0012 foil based semi-active flow energy harvester, where a sinusoidal pitching motion was employed, and the heaving motion was flow induced through a spring-damper system. They found that flapping foils could have a comparative performance over conventional rotary turbines with typical efficiencies up to about 30% but at lower tip speed ratios. Studies have also been conducted to investigate the performance of multi-foil-based flow energy harvesters operating in the semi-active mode, such as Abiru & Yoshitake (2012) and Isogai & Abiru (2012), and confirmed that the multi-foil configuration can help enhance the overall energy extraction performance if an appropriate distance is chosen between foils. Boudreau et al. (2019) numerically investigated a different type of semi-passive flapping foil, i.e., prescribed sinusoidal heaving and passive pitching motions. By varying the system's moments of inertia, pitch stiffness, and location of pivot axis, they obtained energy extraction efficiencies higher than 40% at the Reynolds number of 3.9×10^6 .

In the fully passive mode, both the heaving and pitching motions are induced by the flow, and no actuators are used. This motion mode is common in a classic aeroelastic phenomenon, i.e., wing flutter, and hence has been studied intensively in the aeroelasticity community. However, most of the existing studies were focused on how to mitigate the flutter instability, and only a few looked at the energy extraction by utilizing this instability, e.g., Peng & Zhu (2009), Zhu et al. (2011), Young et al. (2013), Veilleux & Dumas (2017), Picard-Deland et al. (2019) and Jiang et al. (2020). In these studies, the foil was usually mounted on a supporting structure consisting of a torsion spring, a linear spring and a linear damper, oscillating in two degrees of freedom. Recently, Boudreau et al. (2018) conducted an experimental investigation on this concept in a water channel at the Reynolds number of 21,000 and found that the energy harvesting efficiency and power coefficient can be up to 31% and 0.86, respectively. Furthermore, this good performance can be attained over a wide range of flow and structural parameters, which is important in practical applications. They further investigated the performance of this system using numerical simulations, where a maximum efficiency of 53.8% was achieved (Boudreau et al., 2020). Duarte et al. (2019) also studied this concept with a NACA0015 foil at the Reynold number of 60,000. It was found that the pivot axis must be

located after 29% chord length from the leading edge in order to make the device work. Moreover, their results indicate that increasing the heaving natural frequency can be beneficial for the system performance.

Different from the classical wing-flutter configuration, Platzer and colleagues (Platzer & Sarigul-Klijn, 2009; Platzer & Bradley, 2009) proposed a novel design. Instead of utilizing the flutter instability, they used aerodynamic force/moment to drive the foil along a guide rail and implemented two sets of limiters to constrain its linear and angular motions. In this way the foil can undergo sustainable flapping motion without using any spring. Although promising, they only demonstrated the working principle of this novel design, predicted its power extraction performance, and proposed potential applications. The detailed fluid-structure interaction (FSI) and the influence of key parameters on the resulting power extraction performance have yet been explored.

Aiming at revealing more underlying FSI physics of Platzer and colleagues' design, in this study we first developed a fully passive flapping-foil-based flow energy harvester with necessary alterations, **which, along with the dedicated test methods and performance indicators, are introduced in Section 2.** Then, through a series of water-tunnel experiments we studied this test model's dynamics and energy extraction performance under various flow and operation conditions. **The analyses and discussions of the test results are presented in Section 3. Last, the major conclusions from this study are drawn in Section 4.** With a profound understanding being obtained, the system can be improved in the near future to achieve better performance.

2. EXPERIMENTAL SETUP

2.1 TEST MODEL

Our test model was built based on the concept proposed by Platzer and colleagues (Platzer & Sarigul-Klijn, 2009; Platzer & Bradley, 2009) as well as the geometric and test conditions of our water tunnel. As shown in Fig. 1(a), it consists of a rigid foil (i.e., a rectangular flat plate) of 140 mm (chord) \times 200 mm (span) \times 5 mm (thickness) and 0.25 kg that is vertically installed on a purely translating platform of 0.9 kg through a long shaft and bearings. The foil is immersed in the water flow, undergoing both heaving and pitching motions when subject to hydrodynamic forces. Driven by the foil through the long shaft, the upper platform undergoes translating motions along two linear guides that were fixed on the water tunnel.

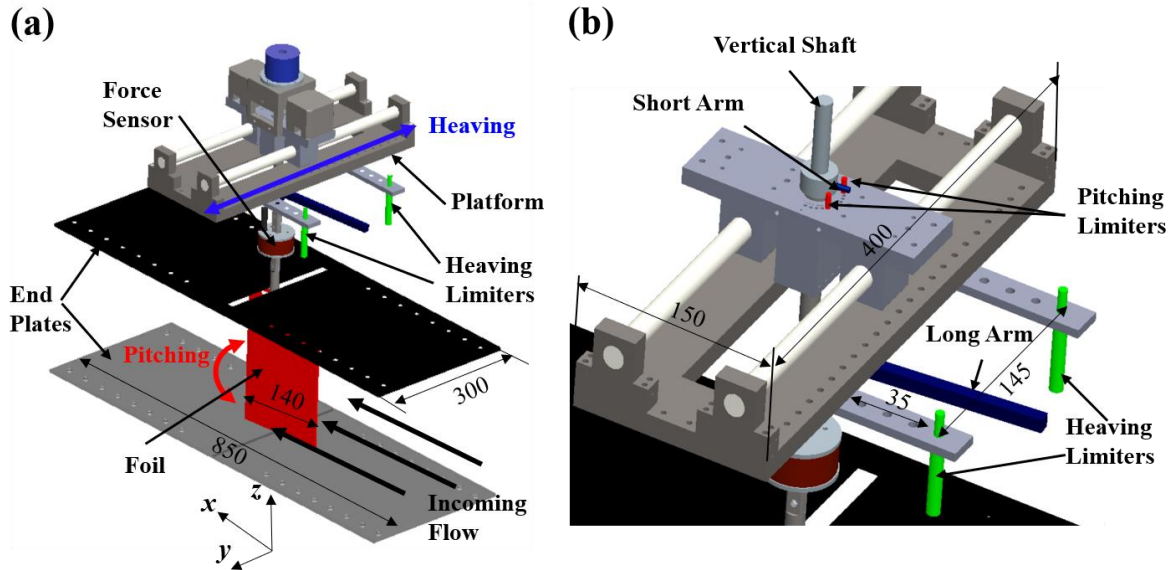


Figure 1 (a) Schematic of the experimental setup that is able to achieve fully passive heaving and pitching motions with the help of two sets of motion limiters; (b) Close-up view of the top part of the setup showing a set of heaving limiters (in green) and a set of pitching limiters (in red). (not to scale, all dimensions in mm)

To enable sustainable heaving and pitching motions, two pairs of motion limiters are employed. As shown in Fig. 1(a), a pair of limiters are installed underneath one of the linear guides, each consisting of an aluminum bar extruding towards the upstream. During the operation of the foil, these limiters periodically contact with a long arm fixed on the vertical shaft of the foil, forcing the foil to rotate and reverse its stroke. In this way they refrain the foil's heaving amplitude, hence are termed "*heaving limiters*". The other pair of limiters are installed near the shaft on the top of the upper translating platform, as shown in Fig. 1(b). They periodically make contacts with a short arm installed on the shaft to refrain the foil's pitching amplitude, hence termed "*pitching limiters*". Both the heaving and pitching limiter pairs are designed in such a way that their locations are adjustable, so that the performance of the test model can be studied with pre-defined heaving and pitching ranges.

Note that, our test model does not contain any actuator, which means it is designed to undergo fully passive heaving and pitching motions in water flows. **In addition, there is no mechanical linkage to connect the foil's heaving and pitching motions, which makes our model essentially different from most existing fully passive, non-flutter type devices, such as in McKinney & DeLaurier (1981), Jones et al. (1999) and Xu et al. (2017).**

2.2 MEASUREMENTS

The model was tested in our closed-circuit water tunnel, which has a test section of $2.0 \text{ m} \times (\text{L}) \times 0.3 \text{ m} (\text{W}) \times 0.6 \text{ m} (\text{H})$ and can generate a uniform water flow of speed up to 1 m/s . To eliminate the three-dimensional effect in the flow near the foil tips, a set of acrylic end plates were deployed along the upper and lower edges of the foil with a small clearance of approximately 3.5 mm , as shown in Fig. 1(a). The bottom end plates are transparent to allow optical measurement, whereas the top end plates are made of black acrylic sheets to provide a black background for optical measurements.

To study the interactions between the flapping foil and its surrounding water flow, as well as to evaluate the energy harvesting performance of the test model, a set of measurement techniques were employed to measure the foil's kinematics and the forces/torques it experienced. First, a high-speed camera (Photron Mini UX100) operating at 125 fps was used underneath the water tunnel to capture the foil's heaving and pitching motions. To facilitate this measurement, the bottom edge of the foil was marked with two white dots: one close to the leading edge and the other close to the trailing edge. The images obtained from the camera were then processed to determine the foil's linear and angular displacements, velocities and accelerations. Second, a six-component load cell (ATI Mini-40) was used to measure the forces/torques experienced by the foil with a sampling rate of 2000 Hz , which was installed on the vertical shaft and located between the foil and the upper translating platform, as shown in Fig.1(a). The camera and the load cell were synchronized using a LabView virtual instrument through a DAQ chassis (NI cDAQ 9174). The generated data were then collected by a computer through the same DAQ chassis. To remove high-frequency noises, the force/torque data obtained from the load cell were processed by a low-pass filter with a cut-off frequency of 10 Hz .

The surrounding flow field was measured using a time-resolved particle image velocimetry (TR-PIV) system. As depicted in Fig. 2, a laser sheet of about 1 mm thickness is produced from a 10 W continuous-wave laser generator (CNI PSU-W-LED), aligned with the foil's mid-span plane. The water flow was seeded with polyamide particles of $50 \mu\text{m}$ diameter (Dantec Dynamics PSP-50). The lights reflected from these particles in a field of view of $1.7c$ (streamwise) \times $1.8c$ (spanwise), where c is the chord, were collected by the high-speed camera (Photron Mini UX100) with a Nikon 105 mm lens from the bottom side through a mirror placed at 45° with the horizontal plane. The camera was operated at 1000 fps , high enough to resolve

the foil's flapping cycles. Images from about 50 flapping cycles were acquired for each case studied herein. These images were processed using Dantec's DynamicStudio to produce velocity vectors. The adaptive PIV technique was adopted with the minimum and maximum interrogation areas 16×16 pixels and 32×32 pixels, respectively.

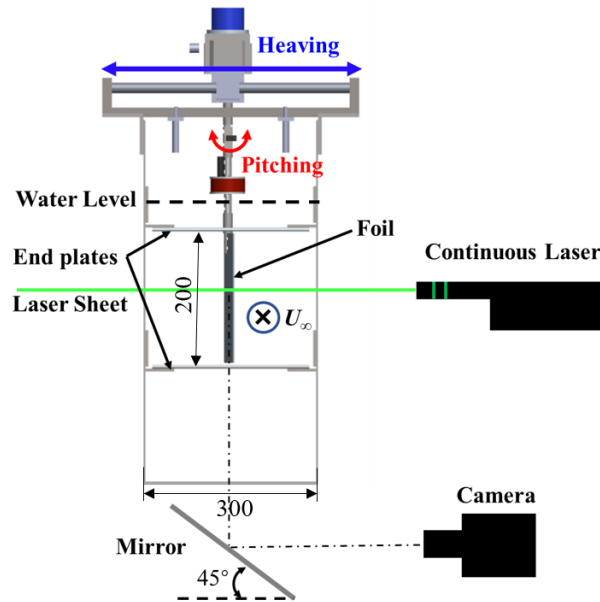


Figure 2: Schematic of the TR-PIV measurements. A laser sheet of about 1 mm thickness is produced through a set of optic lenses from a laser generator. The instantaneous foil motion and lights reflected from tracer particles are recorded using a high-speed camera operating at 1000 fps through a mirror placed underneath the water tunnel. (not to scale, all dimensions in mm)

The uncertainty in the image-based motion measurements was estimated as 0.5%. The force/torque measurements were calibrated using a dead weight and the uncertainties are about 1.5% and 1.25%, respectively. As the PIV measurements, the major uncertainty source came from the root-mean-square fluctuation of the particle displacement in PIV images, which was estimated to be about 0.08 pixel (Willert & Gharib 1991). As a result, the measurement uncertainties induced by the recursive image integration procedure are 2% ~ 5%. The vorticity was calculated in the velocity field using a standard central difference scheme. Its uncertainty e_ω was estimated from the uncertainty in velocity e_u using the formula $e_\omega = (u_{\max} \cdot e_u / \Delta x) / \omega_{\max}$, where Δx is the grid size, u_{\max} the maximum velocity, and ω_{\max} the maximum vorticity. With this formula, the uncertainty for the resulting vorticity is estimated to be about 4% ~ 10% of the maximum vorticity in the field.

2.3 PERFORMANCE ASSESSMENT

Note that, our test model only converts the flow kinetic energy into the model's mechanical energy and does not further convert the latter to electric energy by utilizing any power take-off system. Hence in this study the model's energy harvesting performance was analyzed and evaluated based on the energy transfer from the flow kinetic energy to the model's mechanical energy, through investigating the associate fluid-structure interactions (FSI).

To facilitate the analysis, a Cartesian coordinate system is defined, with its origin located at the intersection point of the foil's mid-span plane, the long shaft's sweeping plane and the water tunnel's plane of symmetry, its x axis along the streamwise direction, y axis along the transverse direction, and z axis along the vertical direction, as depicted in Fig. 1(a). In addition, a body-fixed coordinate system is defined in such a way that its x' and y' axes are in the foil's min-span plane, along and normal to the chord, respectively.

Since the load cell rotates together with the foil, it reads forces/moments along the body-fixed axes, i.e., $F_{x'}$, $F_{y'}$, $M_{z'}$. Their transverse and vertical components, i.e., F_y and M_z , can then be evaluated by applying coordinate transformations

$$F_y = F_{y'} \cos \theta + F_{x'} \sin \theta \quad (1)$$

$$M_z = M_{z'} \quad (2)$$

where θ is the foil's pitching angle read from the synchronized high-speed camera. Note that, the above force and moment include two components: the hydrodynamic force exerted on the foil and the inertial force of the moving foil. By subtracting the inertial force in y direction, the transverse hydrodynamic force, F_h , can be obtained as

$$F_h = F_y - m\ddot{h} \quad (3)$$

where m is the total mass of the foil and the portion of the long shaft underneath the load cell (0.20 kg), and \ddot{h} is the foil's heaving acceleration in y direction. Note F_h is the lift force experienced by the foil. Similarly, by subtracting the inertial moment in z direction, the hydrodynamic pitching moment, M_θ , can be evaluated as

$$M_\theta = M_z - I_z \ddot{\theta} \quad (4)$$

where I_z is the mass moment of inertia of the foil and the portion of the long shaft underneath the load cell about z axis, which is dependent on the location of the long shaft, and $\ddot{\theta}$ is the

foil's pitching acceleration. By non-dimensionalizing F_h and M_θ using the foil and freestream properties, we get the coefficients for heaving force and pitching moment

$$C_h = \frac{F_h}{\rho U_\infty^2 b c / 2} \quad (5)$$

$$C_\theta = \frac{M_\theta}{\rho U_\infty^2 b c^2 / 2} \quad (6)$$

where ρ is the fluid density, U_∞ is the freestream velocity, and b and c are the foil's span and chord, respectively.

Once the foil's motions and hydrodynamic force/moment are obtained, the system's power extraction can be evaluated as

$$P = P_h + P_\theta = F_h \dot{h} + M_\theta \dot{\theta} \quad (7)$$

where P is the total power, the summation of P_h , the power conversion by the heaving motion, and P_θ , the power conversion by the pitching motion. \dot{h} and $\dot{\theta}$ is the foil's heaving velocity and pitching velocity, respectively. Nondimensionalizing these powers using the foil and freestream properties gives the corresponding power coefficients

$$C_p = C_{ph} + C_{p\theta} = \frac{F_h \dot{h}}{\rho U_\infty^3 b c / 2} + \frac{M_\theta \dot{\theta}}{\rho U_\infty^3 b c / 2} = C_h \frac{\dot{h}}{U_\infty} + C_\theta \frac{\dot{\theta} c}{U_\infty} \quad (8)$$

where C_p is the total power coefficient, the summation of C_{ph} , the power coefficient of the heaving motion, and $C_{p\theta}$, the power coefficient of the pitching motion.

Note that, the force, power and their coefficients introduced above are all time dependent quantities, which were evaluated using phase-averaged forces and displacements measured by the load cell and high-speed camera over 50 flapping cycles. To assess the overall performance of the system, the time averaged power coefficient, \bar{C}_p , can be evaluated as

$$\bar{C}_p = \frac{1}{T} \int_t^{t+T} C_p dt = \bar{C}_{ph} + \bar{C}_{p\theta} \quad (9)$$

where T is the foil's flapping period. \bar{C}_{ph} and $\bar{C}_{p\theta}$ are the time averaged power coefficients due to the heaving motion and the pitching motion, respectively. The overall efficiency of the energy harvesting, η , is defined as the ratio of the mean power to the power carried in the flow through the frontal area of the foil

$$\eta = \frac{\bar{P}}{\rho U_\infty^3 b h_0} = \frac{c}{2h_0} \bar{C}_p \quad (10)$$

where \bar{P} is the time averaged power, and h_0 is the foil's heaving amplitude defined as a half of the sweep distance of the foil's pivot axis. Since in the present study both c is a constant and h_0 varies very little in different cases, \bar{C}_p and η are generally equivalent and hence we only use \bar{C}_p to indicate the overall performance of the system.

2.4 CASE SUMMARY

The test conditions in the present study are summarized in Table 1. The general dynamics and resulting power extraction of the test model will firstly be introduced in a baseline case, in which the foil's pivot axis is located at $x_p = 0.7c$ from the leading edge, the pitching amplitude is $\theta_0 = 45^\circ$, and the incoming water speed is $U_\infty = 0.55$ m/s. The effects of pivot location, pitching amplitude and water speed on the foil's power extraction performance are then studied, separately, by varying one of the parameters with the three selected values indicated in Table 1, while keeping the other two fixed at the baseline values. Hence, in total seven different tests were conducted and analyzed.

Table 1: Summary of test conditions (Conditions for the baseline case are marked in bold)

Pivot Location x_p	Pitching Amplitude θ_0	Water Speed U_∞ (m/s)
0.6c, 0.7c , 0.8c	30°, 45° , 60°	0.46, 0.55 , 0.69

3. RESULTS AND DISCUSSION

Before discussing any specific case, we describe the general kinematics of the foil based on our observations. With the implementation of the motion limiters, i.e., a pair of heaving limiters and a pair of pitching limiters, the foil can achieve sustainable flapping motions in uniform water flow and hence convert the flow kinetic energy into the model's mechanical energy. The foil's kinematics can be generally divided into two phases, i.e., the pure heaving phase and the stroke reversal phase. As depicted in Fig. 3, after its stroke reversal at the bottom side, the foil touches one of the pitching limiters, reaching and maintaining its maximum pitching angle at θ_0 . With such a large pitching angle, the resulting heaving force (i.e., F_h) pushes the foil upward until it touches the upper heaving limiter. This defines the pure heaving phase. When touching the upper heaving limiter, the foil is forced to rotate anticlockwise by the upper heaving limiter, reducing its pitching angle. As a result, the foil leaves the confining pitching limiter and enters the stroke reversal phase. In the stroke reversal phase, the foil keeps rotating from $+\theta_0$ to $-\theta_0$

until it touches the other pitching limiter to start the next pure heaving phase. Since the same pure heaving and stroke reversal phases will repeat during the subsequent downstroke, a whole flapping cycle consists of two pure heaving phases and two stroke reversal phases.

If observed in more detail, the stroke reversal phase can be further divided into two stages. Take the upward-to-downward stroke reversal as an example. In the first stage, the foil keeps contacting with the upper heaving limiter and rotating due to the momentum gained in the preceding pure heaving phase. Note that, in this stage since the foil rotates together with its long shaft that moves vertical up along a straight line, the long arm attached on the shaft has to slide on the heaving limiter. This stage ends when the foil starts to leave the heaving limiter, which occurs when the foil's pitching angle becomes negative so that the induced heaving force and pitching moment reverse their directions. After that, driven by the reversed pitching moment (i.e., M_θ), the foil continues rotating anticlockwise until its pitching angle reaches $-\theta_0$ and the foil touches the other pitching limiter. This defines the second stage, in which the foil is not in contact with any limiter. Note that, since in the present study the heaving motion is defined according to the foil's long shaft's translational motion, the foil still undergoes heaving motion during the stroke reversal phase.

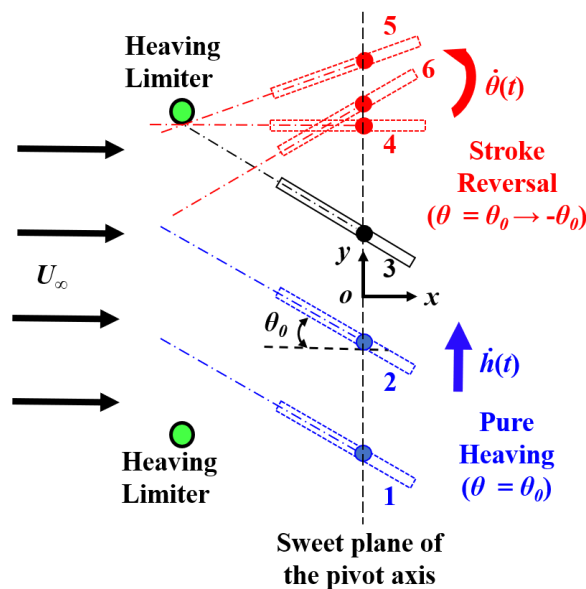


Figure 3: Schematic showing a half of the flapping cycle (a pure upward heaving followed by an upward-to-downward stroke reversal, not in scale). 1-3: pure heaving (in blue); 3-5: first stage of stroke reversal (in red); 5-6: second stage of stroke reversal (in red). The pivot axis of the foil is marked by a solid circle, which sweeps in a vertical plane as represented by a vertical, dashed line. The dot dashed lines indicate the long arm as described in Fig. 1(b).

3.1 A BASELINE CASE

In the baseline case, the corresponding chord-based Reynolds number is $Re = 7.7 \times 10^4$. A video showing the foil's continuous flapping motion can be found in the supplementary material. Figure 4(a) shows the evolution of the foil's phase-averaged linear and angular displacements in one flapping cycle, where $t/T = 0$ is defined as the instant when the foil's pivot axis (i.e., the long shaft) reaches its positive maximum. It is seen that the foil undergoes downstroke from $t/T = 0$ to 0.48 and then upstroke from $t/T = 0.48$ to 1, which is not perfectly symmetric in time. This was caused by the imperfect manufacturing and assembly of the test model. Similarly, the foil's pitching motion is also not symmetric in time. The two pure heaving phases ($t/T = 0.05 \sim 0.25$ and $0.56 \sim 0.74$) are shaded, where the foil's pitching angle is maintained at $\theta = -\theta_0$ and $+\theta_0$, respectively, whereas the two stroke reversal phases are in white background. It is clearly seen that the foil still undergoes significant heaving motion during the stroke reversals.

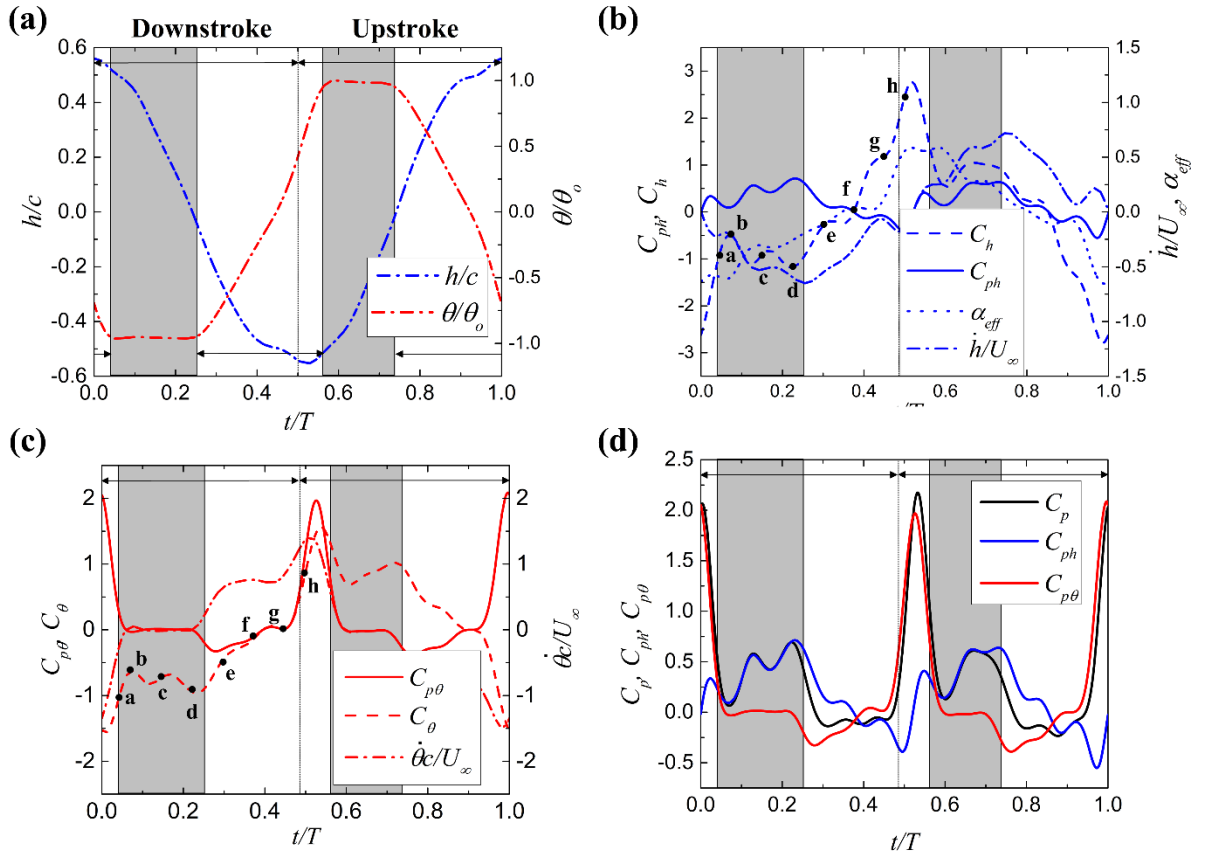


Figure 4: Evolution of phase-averaged quantities in one cycle in the baseline case ($x_p = 0.7c$, $\theta_0 = 45^\circ$, $U_\infty = 0.55$ m/s): (a) heaving displacement h/c and pitching angle θ/θ_0 ; (b) heaving force coefficient C_h , heaving velocity \dot{h}/U_∞ , heaving power coefficient C_{ph} and effective angle of attack α_{eff} ; (c) pitching moment coefficient C_θ , pitching velocity $\dot{\theta}c/U_\infty$, pitching power coefficient $C_{p\theta}$; and (d) heaving power coefficient C_{ph} , pitching power coefficient $C_{p\theta}$, and pitching power coefficient $C_{p\theta}$.

$C_{p\theta}$ and total power coefficient C_p . The total power is dominated by the heaving motion in the pure heaving phases (shaded background). In the stroke reversal phases (white background), the heaving and pitching motions compete roughly in the first half, whereas the pitching motion dominates in the second half. Both the motions are able to make positive contributions to the flow energy harvesting.

Figures 4(b) and 4(c) show the evolution of the velocity, force and power for the heaving motion and pitching motion, respectively. It is observed that the heaving velocity, \dot{h}/U_∞ , reaches its peak or trough at the end of each pure heaving phase, i.e., $t/T = 0.25$ or 0.74 , reflecting that the foil starts decelerating immediately after it touches the heaving limiters. The variation of the heaving velocity is also accompanied by higher-frequency oscillations, which may be caused by obvious jerks and vibrations of the foil system observed during the experiments. Differently, the heaving force coefficient, C_h , peaks at around the end of each stroke reversal, the same instants when the foil reaches its heaving extremes. As the product of C_h and \dot{h}/U_∞ , the heaving power coefficient, C_{ph} , generally repeats twice in one flapping cycle. It is positive roughly in the first half of each stroke, and negative in the second half, as a result of a nearly 90° phase difference between C_h and \dot{h}/U_∞ . In addition, C_{ph} peaks at the end of each pure heaving phase. Hence, the heaving motion mainly extracts the flow energy in the pure heaving phases but consumes energy in the stroke reversal phases. Figure 4(b) also presents the evolution of the foil's mean effective angle of attack, α_{eff} , defined by considering the foil's heaving and pitching motions

$$\alpha_{\text{eff}} = \theta - \arctan \frac{\dot{h} + \dot{\theta} x_{p-3c/4} \cos \theta}{U_\infty - \dot{\theta} x_{p-3c/4} \sin \theta} \quad (11)$$

where $x_{p-3c/4}$ denotes the distance between the foil's pivot axis and its three-quarter-chord point at which the foil rotation does not contribute to circulation (Sane & Dickinson, 2002; Bryant et al., 2013). It is seen that the α_{eff} curve is positively correlated with the C_h curve, indicating that the foil's heaving force is mainly determined by its effective angle of attack.

As shown in Fig. 4(c), the foil's pitching velocity, $\dot{\theta}$, remains almost zero during each pure heaving phase and its magnitude increases during each stroke reversal phase. As for the pitching moment coefficient, C_θ , it varies a lot in the stroke reversal phases, but remains relatively unchanged in the pure heaving phases. Both quantities peak at the end of stroke reversals. As a result, the pitching power coefficient, $C_{p\theta}$, shows a significant peak at the end of stroke reversals. In addition, $C_{p\theta}$ is almost zero during the pure heaving phases, due to the

nearly-zero pitching velocity, and becomes slightly negative at the start of each stroke reversal, indicating that during this short period the pitching motion is absorbing energy from the flow.

As the sum of C_{ph} and $C_{p\theta}$, the evolution of the total power coefficient, C_p , is shown in Fig. 4(d). It is not surprising to see that the total power is dominated by the heaving motion in the pure heaving phases. In the stroke reversal phases, the heaving and pitching motions compete roughly in the first half, leading to slightly negative C_p , whereas the pitching motion dominates in the second half, producing a sharp C_p peak at the end of each stroke reversal.

The foil’s time-averaged performance is listed in Table 2. Both the heaving and pitching motions contribute to the flow energy harvesting, and their contributions are quite close, i.e., 52% from the heaving motion and 48% from the pitching motion. Our test model is able to generate a mean power of $\bar{P} = 0.85$ W, leading to a power conversion efficiency of $\eta = 32.5\%$. However, it should be noted that in this study the power conversion refers to the “*hydrodynamic power extraction efficiency*” rather than “*water-to-wire efficiency*” due to the lack of a power-take-off system.

Table 2: Time-averaged performance of the foil system for the baseline case

\bar{C}_{ph}	$\bar{C}_{p\theta}$	$\bar{C}_p = \bar{C}_{ph} + \bar{C}_{p\theta}$	\bar{P} (W)	η (%)
0.189	0.174	0.363	0.85	32.5

The PIV measurements also revealed the interaction between the flapping foil and its surrounding flow especially vortices. It is seen from Figs. 5(a) to 5(d) that, during the pure downward heaving phase, a clear leading-edge vortex (LEV) forms and sheds, which is followed by the second LEV. These vortices are pushed downward by the downward moving foil, staying close to the foil, creating a low-pressure region near the foil’s leading edge, and hence enhancing the heaving force and pitching moment. This explains the non-decreasing C_h and C_θ appearing in the pure heaving phases (instants b-d) despite the decreasing magnitude in α_{eff} , as revealed in Figs. 4(b) and 4(c). Figures 5(e) to 5(h) show four selected snapshots in the following downward-to-upward stroke reversal. It is seen that the two near-wall vortices are further pushed downward by the foil, inducing a counter rotating secondary vortex that appears near the mid chord of the foil. After the foil reverses its pitching angle, the first LEV wraps around the foil’s trailing edge, as revealed in Fig. 5(g) and also the mirrored image in Fig. 5(a).

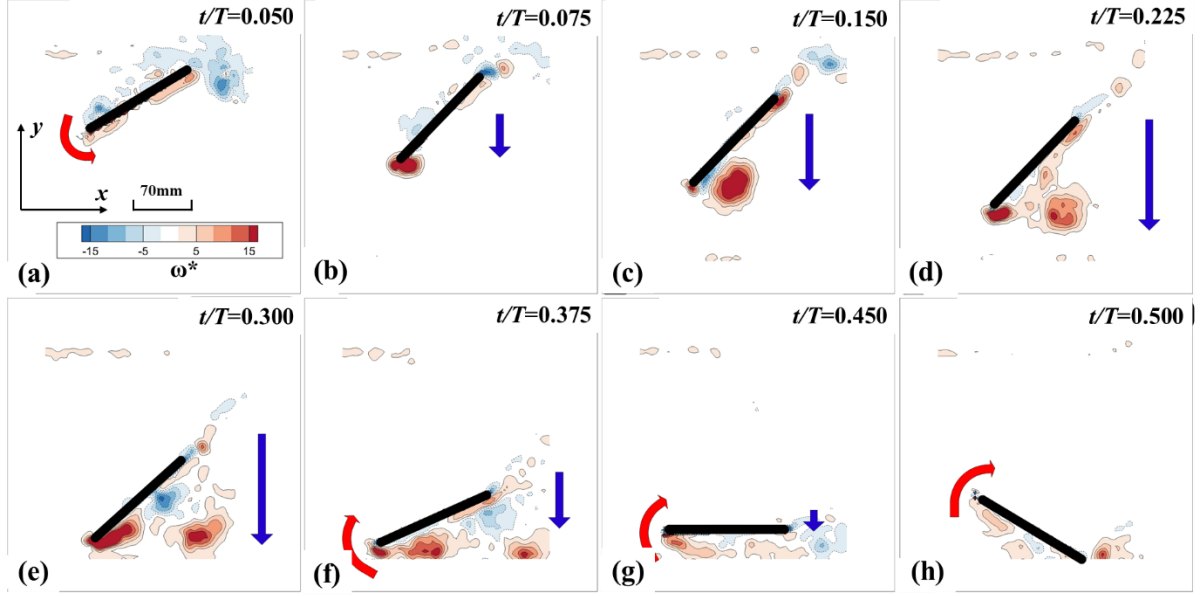


Figure 5: Vortex generation and evolution from the flapping foil in a half flapping cycle. The eight selected instants a-h have been marked in Figs. 4(b) and 4(c). The blue arrow indicates the heaving direction and magnitude, and the red arrow indicates the pitching direction. Two LEVs are generated during the heaving motion, which are then pushed downward by the foil.

3.2 EFFECT OF PIVOT LOCATION

Starting from this section, the effects of three important parameters on the foil's power extraction performance are studied, including the location of the pivot axis, the allowed pitching amplitude and the water speed (refer to Table 1 for the selected values). In the baseline case, the foil's pivot axis is located at $x_p = 0.7c$ from the leading edge. As this axis moves, the foil's power extraction performance will change accordingly. To study the effect of pivot location, in the experiments we varied x_p in the range of $0.6c$ to $0.8c$, while keeping the streamwise distance of the pivot axis from the heaving limiters unchanged (i.e., 105 mm). The corresponding mass moment of inertia I_z is then changed from 2.14×10^{-3} to 2.72×10^{-3} kg·m². As shown in Fig. 6, both the mean heaving power and the mean pitching power increase with x_p . As a result, the total power increases significantly (the highest mean power of about 1 W is achieved at $x_p = 0.8c$), and the power conversion efficiency also increases from 24.7% to 35.2%.

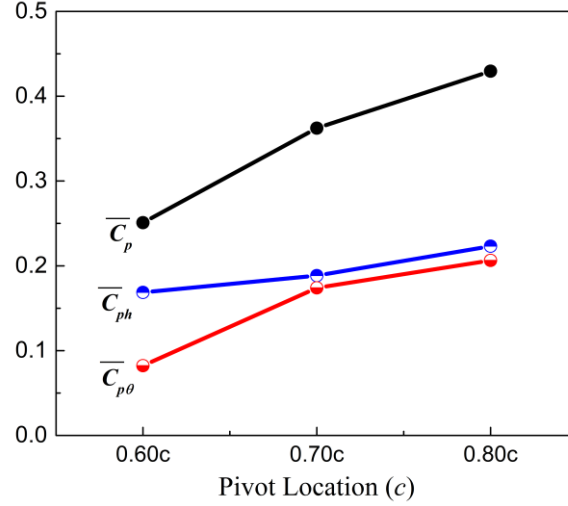


Figure 6: Variations of heaving power coefficient \bar{C}_{ph} , pitching power coefficient $\bar{C}_{p\theta}$ and total power coefficient \bar{C}_p against the pivot location for the flapping foil system with $\theta_0 = 45^\circ$ and $U_0 = 0.55$ m/s. All power coefficients increase as the pivot axis is moved towards the foil's trailing edge.

The foil's dynamics also changes as the pivot location changes. As shown in Fig. 7, the foil's flapping frequency f reduces from 0.67 to 0.60 Hz when x_p increases from $0.6c$ to $0.8c$. This is not surprising because the sweep distance of the pivot axis (i.e., $2h_0$) increases with x_p (as read from Fig. 8(ii)), which requires a longer time to travel. As another key parameter of flapping-foil aerodynamics, the Strouhal numbers in different cases are also compared. Here the Strouhal number is defined as $St = 2h_0f/U_\infty$, which characterizes the ratio of the heaving velocity to the freestream velocity. It is seen from Fig. 7 that, although f reduces, St increases with x_p , indicating that the mean heaving velocity increases as the foil's pivot axis moves towards the trailing edge.

It is interesting to note that the Strouhal number varies in a range of 0.172 to 0.189, lower than the typical values of natural flyers/swimmers at cruising, i.e., $0.2 < St < 0.4$ (Taylor et al., 2003; Triantafyllou et al., 2000). This confirms that for flapping foils the Strouhal number in the energy harvesting mode (i.e., drag production) such as in the present study is generally lower than that in the energy consumption mode (i.e., thrust production) adopted by natural flyers/swimmers, which is consistent with the findings reported by Xiao et al. (2014).

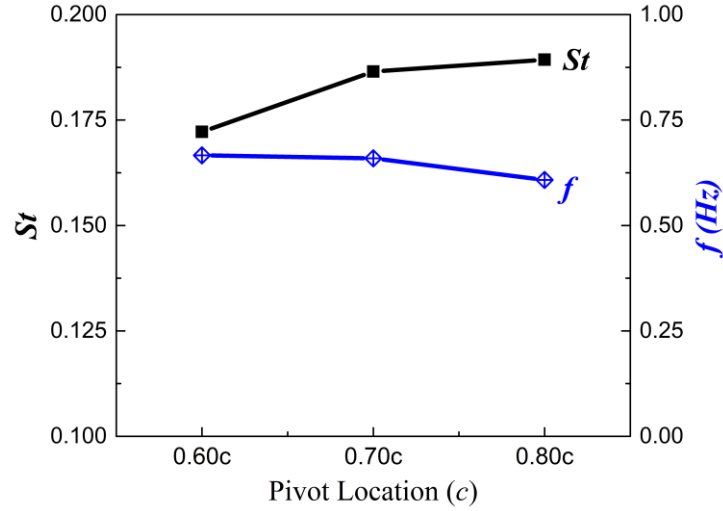


Figure 7 Variation of flapping frequency f and Strouhal number St against the pivot location for the flapping foil system at $\theta_o = 45^\circ$ and $U_\infty = 0.55$ m/s. As the pivot axis is moved towards the foil's trailing edge, the flapping frequency reduces, whereas the Strouhal number increases due to the increase of sweep distance.

To elaborate why the harvested power increases with x_p , Fig. 8 compares the evolution of the foil's displacements, velocities, forces/moments and powers in one flapping cycle for the three cases. It is seen that, with the increase of x_p , the heaving amplitude increases (see Fig. 8(i)), and the stroke reversal ends earlier (see Fig. 8(ii)). The latter indicates the increase of pitching velocity $\dot{\theta}$, as confirmed in Fig. 8(viii), which further causes the increase of effective angle of attack α_{eff} at the end of stroke reversals (see Fig. 8(iii)). It is also expected that, as x_p increases, i.e., the foil's pivot axis moves towards the trailing edge, the C_θ magnitude generally increases due to the increase of moment arm. This has been confirmed by the result shown in Fig. 8(vii). The increase in C_θ then results in the increase of $C_{p\theta}$, especially at the end of stroke reversals, as revealed in Fig. 8(ix). As for the heaving force C_h shown in Fig. 8(iv), although its peak/trough changes with x_p , this change does not affect the heaving power because the corresponding heaving velocities are almost zero. With the above observations, it can be summarized that, as x_p increases, the increase in the total power C_p is mainly due to the increase of $C_{p\theta}$ at the end of stroke reversals plus the increase of C_{ph} at the end of pure heaving, as revealed in Fig. 8(x).

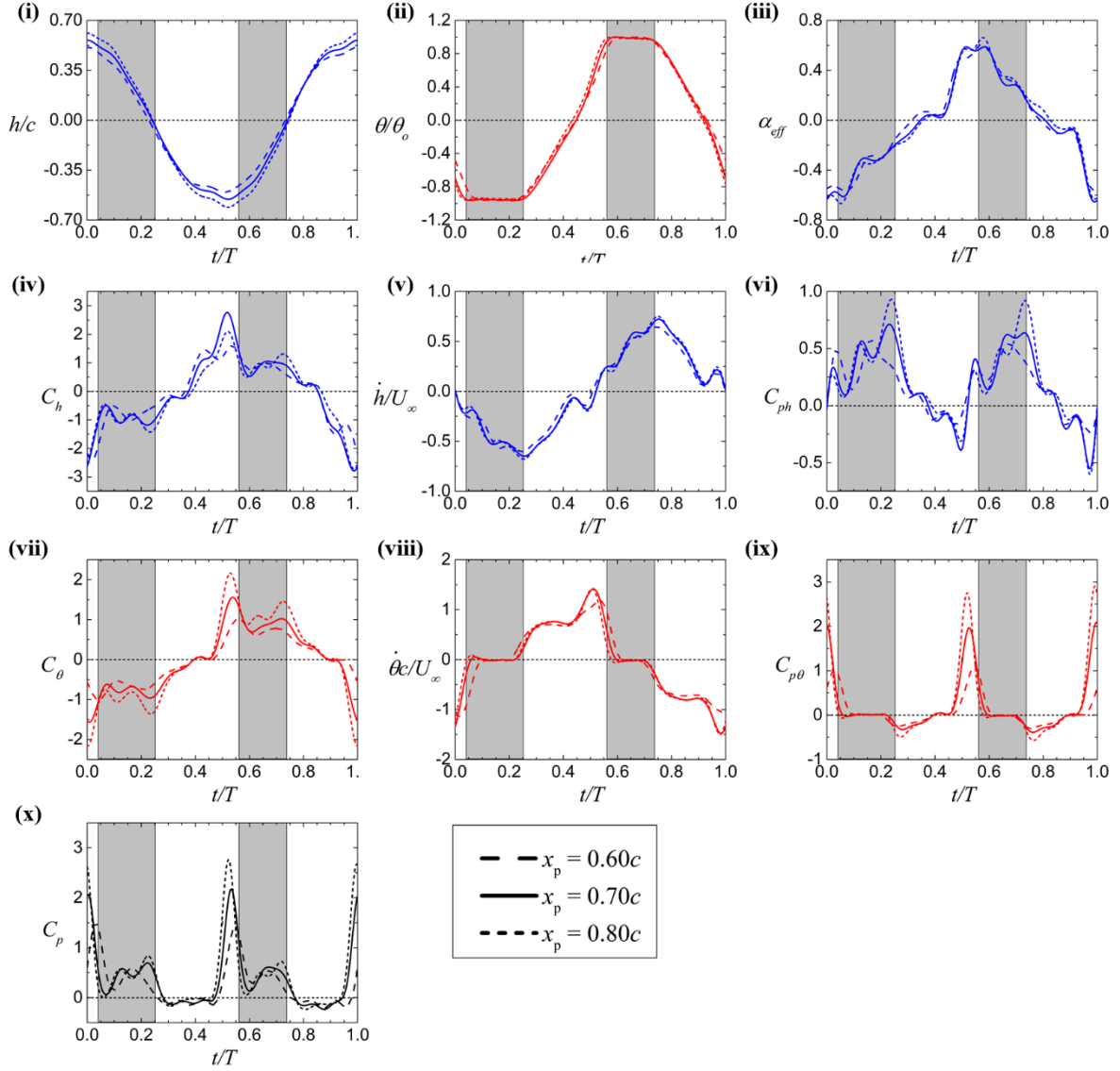


Figure 8 Evolution of phase-averaged quantities for the flapping foil system operating with selected pivot locations at $\theta_0 = 45^\circ$ and $U_\infty = 0.55$ m/s: (i) heaving displacement h/c ; (ii) pitching angle θ/θ_0 ; (iii) effective angle of attack α_{eff} ; (iv) heaving force coefficient C_h ; (v) heaving velocity \dot{h}/U_∞ ; (vi) heaving power coefficient C_{ph} ; (vii) pitching moment coefficient C_θ ; (viii) pitching velocity $\dot{\theta} c/U_\infty$; (ix) pitching power coefficient $C_{p\theta}$; and (x) total power coefficient C_p . The shaded background represents pure heaving phases for the baseline case ($x_p = 0.7c$), whereas the white background represents stroke reversals.

In the experiments we also observed that the test model could not work in a sustainable way if its pivot axis is located at or ahead of about $0.3c$ (A video provided in the supplementary material shows that the test model is able to work continuously at $x_p = 0.35c$, while it barely works at $x_p = 0.3c$), which is consistent with previous observations reported by Duarte et al. (2019). This phenomenon is believed to be associated with the relative position of the foil's hydrodynamic center of pressure from the pivot axis. To ensure continuous flapping, the center of pressure must be located ahead of the pivot axis, i.e., $x_{cp} - x_p < 0$, so that the resulting

hydrodynamic forces/moment can force the foil to maintain contact with the pitching limiter during pure heaving phases and rotate towards the pitching extremes during the second stage of stroke reversals. For the flapping flat plate in the present study, its hydrodynamic center of pressure changes with time, which can be evaluated using the data read from the load cell by the formula $x_{cp} = x_p - M_{\theta}/(F_h \cos\theta + F_x \sin\theta)$. Figure 9 clearly confirms that $x_{cp} - x_p < 0$ during the pure heaving phases and the second stage of stroke reversals for the three cases. Note that $x_{cp} - x_p > 0$ during the first stage of stroke reversals. To overcome this adverse condition, it requires the system to have enough inertia so that the foil can continuously turn and revert the sign of its pitching angle.

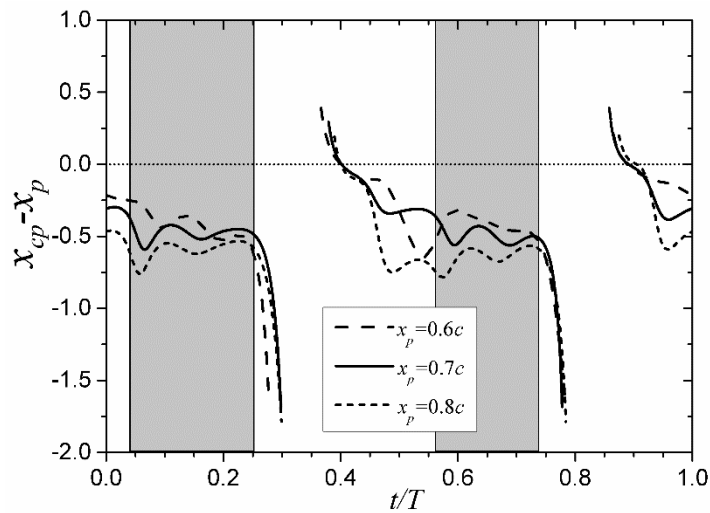


Figure 9: Evolution of the distance between the foil's center of pressure from its pivot location (i.e., $x_{cp} - x_p$) in one flapping cycle. $\theta_0 = 45^\circ$ and $U_\infty = 0.55$ m/s. The shaded background represents pure heaving phases for the baseline case ($x_p = 0.7c$), whereas the white background represents stroke reversals. For the three cases, the foil's center of pressure is far ahead of the pivot axis, i.e., $x_{cp} - x_p < 0$, during the pure heaving phases and the second stage of stroke reversals, which is required for the system to achieve sustainable flapping motion.

3.3 EFFECT OF PITCHING AMPLITUDE

As described in Sec. 2.1, the pitching amplitude of the flapping foil, θ_0 , can be pre-determined using the two pitching limiters. In this section the effect of θ_0 is studied by adjusting these limiters. As shown in Fig. 10, both the mean heaving power \bar{C}_{ph} and the mean pitching power $\bar{C}_{p\theta}$ increase as θ_0 increases from 30° to 60° . As a result, the total mean power \bar{C}_p and the total power conversion efficiency η also increase, with the latter reaching 35.6% at $\theta_0 = 60^\circ$.

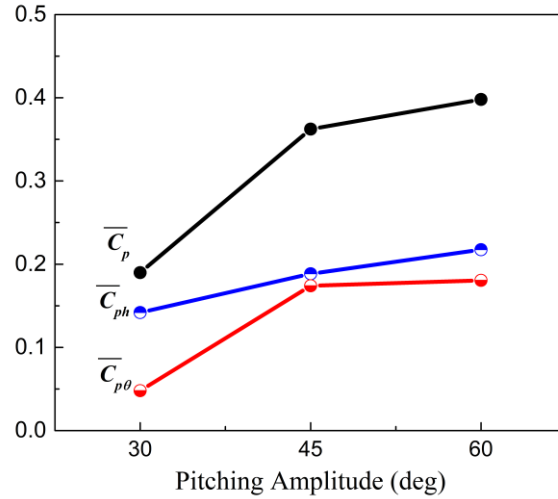


Figure 10 Variations of heaving power coefficient \bar{C}_{ph} , pitching power coefficient $\bar{C}_{p\theta}$ and total power coefficient \bar{C}_p against the pitching amplitude for the flapping foil system with $x_p = 0.7c$ and $U_0 = 0.55$ m/s. All power coefficients increase as the pitching amplitude is increased.

The change in pitching amplitude also affects the foil's dynamics. Different from the powers and efficiencies, however, the Strouhal number does not show a monotonic variation trend, as revealed in Fig. 11. Instead, it increases significantly from 0.145 to 0.187 when θ_0 increases from 30° to 45° , and then decreases to 0.174 when θ_0 further increases to 60° . Since the heaving distances in these three cases do not differ too much, this variation in St is mainly caused by

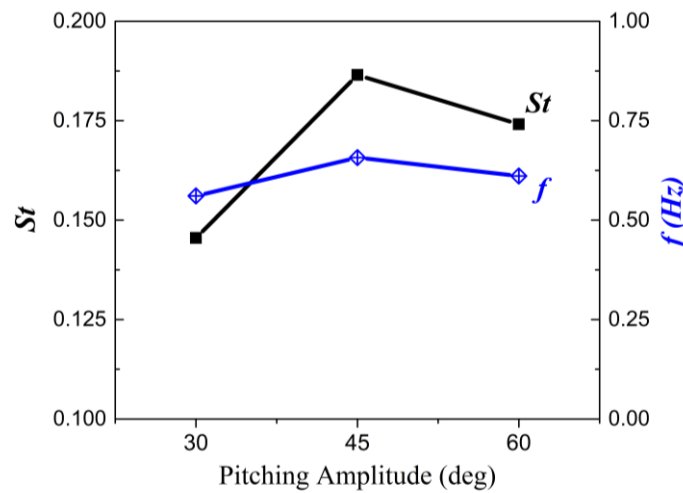


Figure 11 Variation of flapping frequency f and Strouhal number St against the pitching amplitude for the flapping foil system at $x_p = 0.7c$ and $U_\infty = 0.55$ m/s. Maximum flapping frequency and Strouhal number appear when the system operates with an intermediate pitching amplitude.

the change of flapping frequency. On one hand, as the pitching amplitude is set small such as $\theta_0 = 30^\circ$, the heaving force is small leading to a smaller flapping frequency of $f = 0.561$ Hz. On

the other hand, as the pitching amplitude is set large such as $\theta_0 = 60^\circ$, it requires a much longer time to complete the stroke reversals, also leading to a smaller flapping frequency of $f = 0.610$ Hz. Hence, a peak frequency appears at intermediate pitch amplitudes such as $\theta_0 = 45^\circ$.

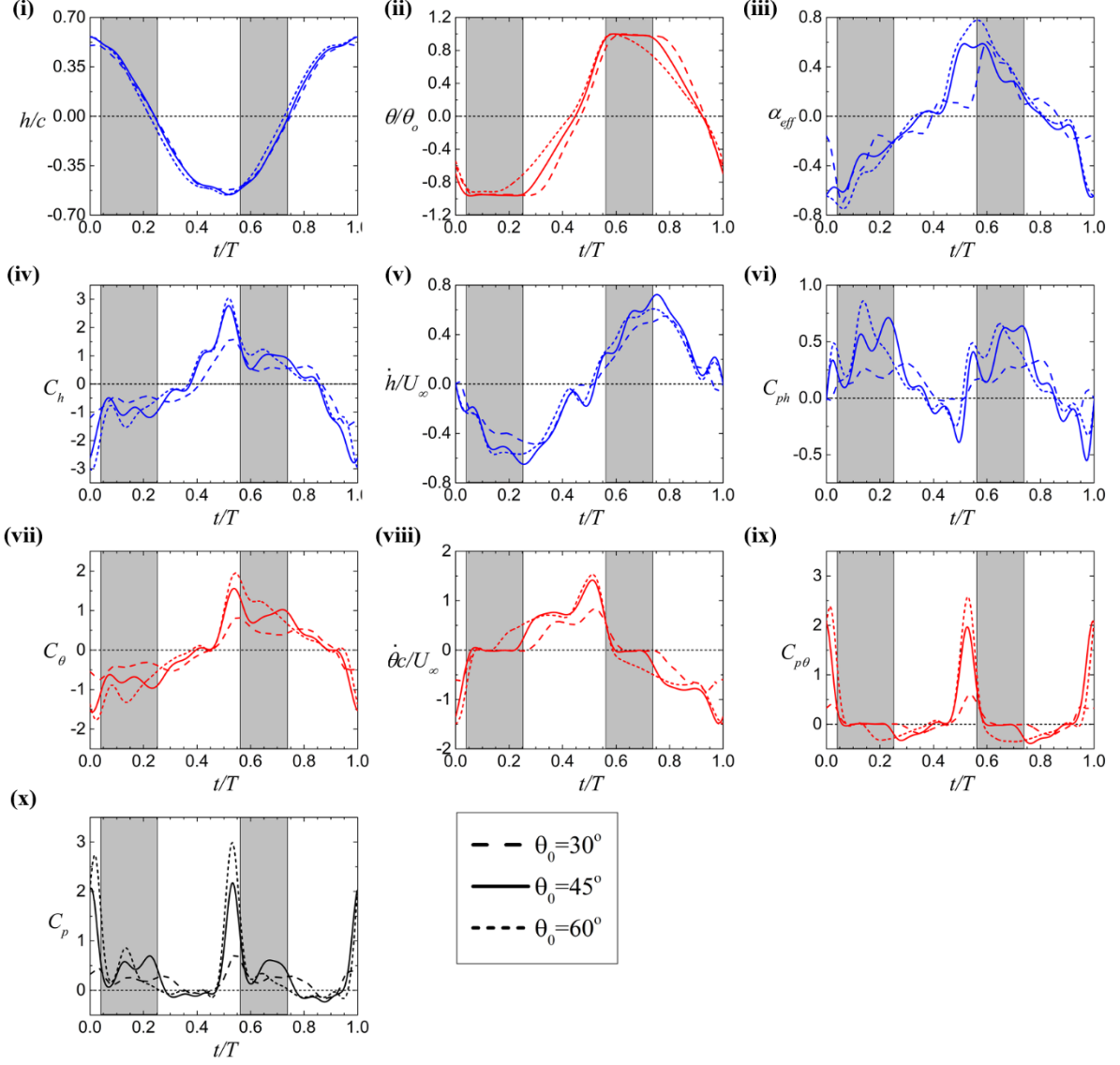


Figure 12: Evolution of phase-averaged quantities for the flapping foil system at selected pitching amplitudes at $x_p = 0.7c$ and $U_\infty = 0.55$ m/s: (i) heaving displacement h/c ; (ii) pitching angle θ/θ_0 ; (iii) effective angle of attack α_{eff} ; (iv) heaving force coefficient C_h ; (v) heaving velocity \dot{h}/U_∞ ; (vi) heaving power coefficient C_{ph} ; (vii) pitching moment coefficient C_θ ; (viii) pitching velocity $\dot{\theta} c/U_\infty$; (ix) pitching power coefficient $C_{p\theta}$; and (x) total power coefficient C_p . The shaded background represents pure heaving phases for the baseline case ($\theta_0 = 45^\circ$), whereas the white background represents stroke reversals.

The evolution of the foil's displacements, velocities, forces/moments and powers in a flapping cycle is presented in Fig. 12. It is seen that, compared with the heaving motion, the pitching motion changes a lot: as θ_0 increases, the pure heaving phases last for a shorter time, which

leads to longer stroke reversal phases, as revealed in Fig. 12(ii). As such, at higher θ_0 the foil rotates in a longer time (see Fig. 12(viii)). On the other hand, higher θ_0 also induces higher pitching moment as confirmed in Fig. 12(vii). These two factors result in much larger pitching power, especially at the end of stroke reversals (Mumtaz Qadri et al., 2019), as shown in Fig. 12(ix). However, due to their out-of-phase relation at the first half of stroke reversals, significant negative pitching power is also obtained in the cases with $\theta_0 = 45^\circ$ and 60° .

The increase in θ_0 also changes α_{eff} , as shown in Fig. 12(iii). This results in the increase of heaving force, as revealed in Fig. 12(iv). As such, the heaving power is also enhanced, especially in the mid strokes. With both the time-varying heaving and pitching powers being enhanced, the total power further increases with θ_0 as confirmed in Fig. 12(x).

3.4 EFFECT OF WATER SPEED

In the experiments a minimum water speed or cut-in speed, i.e., $U_\infty = 0.45$ m/s, was observed, under which the test model could not achieve sustainable flapping motions in a fully passive way. In this section, the performance of the test model is further compared in water flows at three different speeds, i.e., $U_\infty = 0.46, 0.55$ and 0.69 m/s, corresponding to the Reynolds number $6.4 \times 10^4, 7.7 \times 10^4$ and 9.7×10^4 , respectively.

Figure 13 shows the variations of the mean power against the water speed. It is seen that the mean pitching power $\bar{C}_{p\theta}$ monotonically increases with U_∞ , whereas the mean heaving power \bar{C}_{ph} remains almost constant at 0.46 and 0.55 m/s and decreases at 0.69 m/s. As a result, the total mean power \bar{C}_p first increases and then slightly decreases, indicating the existence of an optimal flow speed in this flow range. Although not presented here, it should be noted that the actual power monotonically increases with U_∞ , reaching 1.6 W at 0.69 m/s.

The foil's flapping frequency also increases with the water speed, as shown in Fig. 14, due to the increase of heaving and pitching velocities (as can be read from Figs. 15(iv) and 15(vii)). Despite the increase of water speed, the increase of flapping frequency also leads to the increase of the Strouhal number.

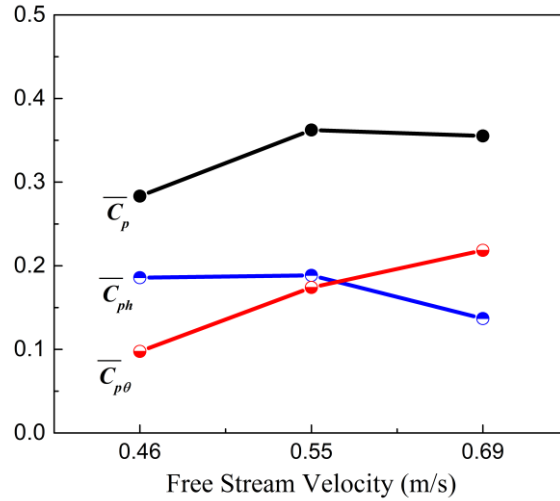


Figure 13: Variations of heaving power coefficient \overline{C}_{ph} , pitching power coefficient $\overline{C}_{p\theta}$ and total power coefficient \overline{C}_p against the freestream velocity for the flapping foil system with $x_p = 0.7c$ and $\theta_0 = 45^\circ$. As the flow speed increases, the heaving power reduces, whereas the pitching power increases. Hence an optimum flow speed appears for the total power.

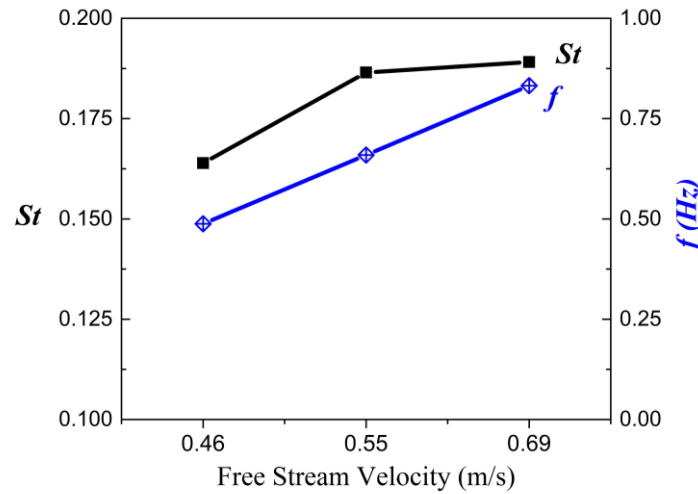


Figure 14: Variation of flapping frequency f and Strouhal number St against the freestream velocity for the flapping foil system at $x_p = 0.7c$ and $\theta_0 = 45^\circ$. Both the flapping frequency and the Strouhal number increase with the flow speed.

Figure 15 shows the evolution of the foil's displacements, velocities, forces/moments and powers in one flapping cycle. The increase of the water speed brings an obvious change: the stroke reversal phase ends earlier as revealed in Fig. 15(ii), reflecting faster stroke reversals. The faster stroke reversal then induces higher pitching velocities and earlier velocity peaks (see Fig. 15(viii)), as well as earlier pitching moment peaks (see Fig. 15(vii)), all occurring at the end of stroke reversals. All these lead to earlier peaks for the pitching power, as shown in Fig. 15(ix). Meanwhile, the higher pitching velocity result in a higher and earlier α_{eff} peak, as

revealed in Fig. 15(iii), which then induces a higher and earlier peak for heaving force (see Fig. 15(iv)). However, it seems the faster stroke reversal does not affect the heaving displacement and velocity too much, as revealed in Fig. 15(i) and 15(v). In addition, the faster water speed does not consistently generate higher peaks for heaving velocity. As a result, the heaving power is not affected significantly, except for the increased negative power appearing at the end of stroke reversals. As the sum of the heaving and pitching powers, the total power is then majorly affected through the phase and magnitude changes at the end of stroke reversals.

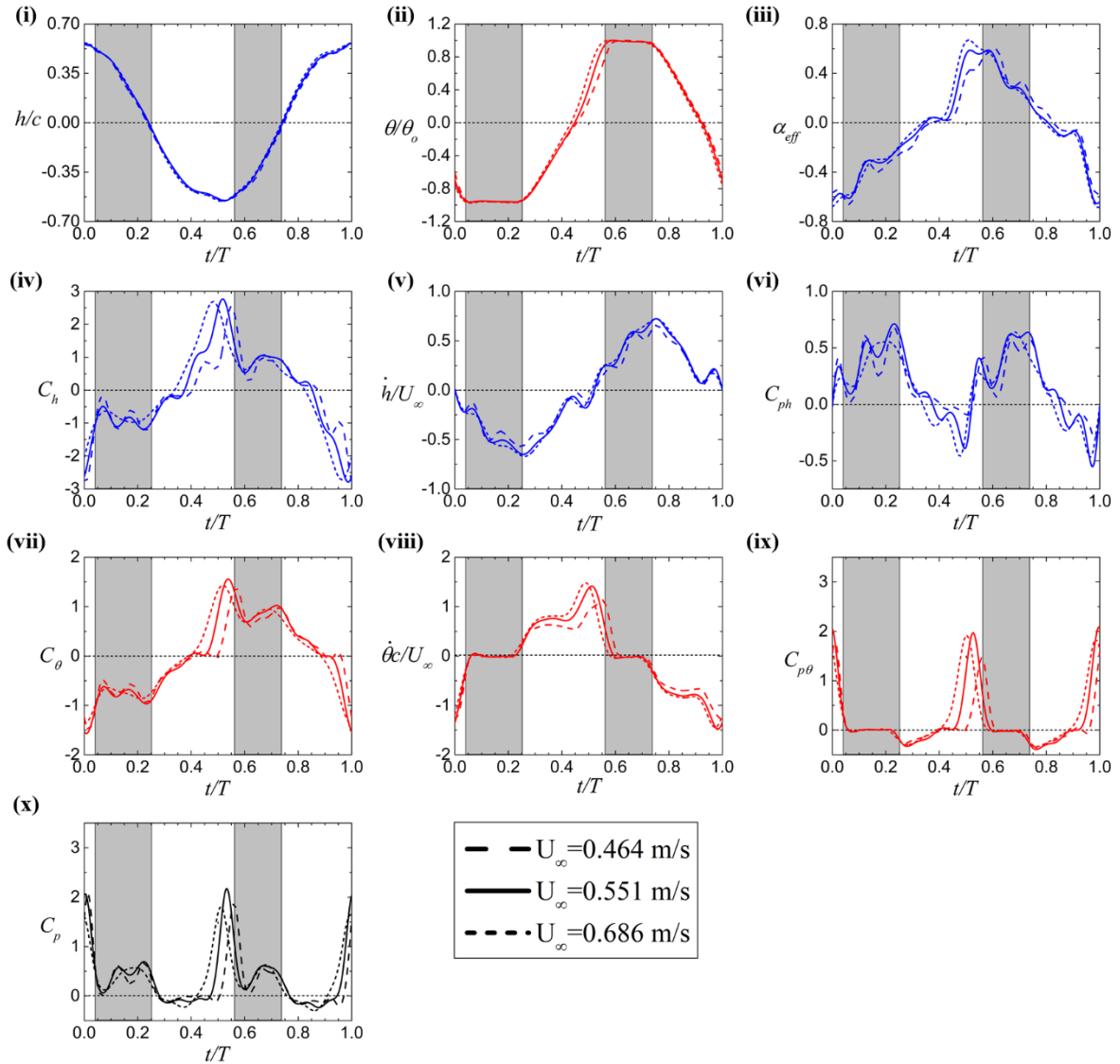


Figure 15 Evolution of phase-averaged quantities for the flapping foil system at selected freestream velocities at $x_p = 0.7c$ and $\theta_0 = 45^\circ$: (i) heaving displacement h/c ; (ii) pitching angle θ/θ_0 ; (iii) effective angle of attack α_{eff} ; (iv) heaving force coefficient C_h ; (v) heaving velocity \dot{h}/U_∞ ; (vi) heaving power coefficient C_{ph} ; (vii) pitching moment coefficient C_θ ; (viii) pitching velocity $\dot{\theta} c/U_\infty$; (ix) pitching power coefficient $C_{p\theta}$; and (x) total power coefficient C_p . The shaded background represents pure heaving phases for the baseline case ($U_\infty = 0.55$ m/s), whereas the white background represents stroke reversals.

4. CONCLUSIONS

In this study we experimentally investigated a novel flapping-foil based flow-energy harvester, which is able to extract energy from water flows through the foil's fully passive flapping motion, i.e., the foil's heaving and pitching motions are not prescribed. The foil's dynamics and energy extraction performance were studied under various flow and operating conditions. The major findings are as follows:

- (1) With the implementation of a pair of heaving limiters and a pair of pitching limiters, the test model is able to achieve sustainable, fully passive flapping motion so as to harvest energy from the surrounding flow. It can generate a mean power of about 1 W in a water flow of $U_\infty = 0.55$ m/s, leading to a power conversion efficiency of 32.5%, **which is similar to 32% reported in Platzner & Sarigul-Klijn (2009), and better than other fully passive, non-flutter type devices, i.e., 28.3% in McKinney & DeLaurier (1981), 26% in Jones et al. (1999) and 25% Xu et al. (2017). Furthermore, the maximum efficiency we obtained in our tests, 35.2%, is even comparable with the most efficient modern turbines which capture around 35~45% of available flow energy (Dunmon et al. 2011).**
- (2) The heaving velocity \dot{h}/U_∞ reaches its extremes at the end of each pure heaving phase, whereas the heaving force C_h reaches its extremes at around the end of each stroke reversal, leading a phase difference of nearly 90° . As such, the heaving power C_{ph} is positive in the pure heaving phases but negative in the stroke reversal phases. Both pitching velocity $\dot{\theta}/U_\infty$ and pitching moment C_θ peak at the end of stroke reversals. Hence the pitching power $C_{p\theta}$ shows a significant peak at the end of stroke reversals.
- (3) The total power is dominated by the heaving motion in the pure heaving phases. In the stroke reversal phases, the heaving and pitching motions compete roughly in the first half, whereas the pitching motion dominates in the second half. Both the motions are able to make positive contributions to the flow energy harvesting.
- (4) As the foil's pivot axis is moved towards the trailing edge, both the mean heaving power and the mean pitching power increase. As a result, the total power increases significantly. The same trend was also observed when the foil's pitching amplitude increases from 30° to 60° . On the contrary, it seems that there exists an optimal water speed between $U_\infty = 0.46$ and 0.69 m/s, at which the power conversion efficiency is maximum.

Note that, our test model has a cut-in speed of $U_\infty = 0.45$ m/s. Although it can be made further smaller by fine tuning the system, the existence of this speed reflects that this type of devices cannot work properly in flows of too low speeds. On the other hand, as the water speed increases, the flapping frequency increases accordingly, as evident in Fig. 14. This may cause serious problems in structural integrity. Therefore, this type of devices cannot work properly in flows of too high speeds either, unless the concern on structural integrity can be well addressed.

In the near future, we will continue studying the effects of other important parameters, such as the heaving amplitude and the streamwise distance between the long shaft and the heaving limiters. In addition, since our test model only converts the flow kinetic energy into the model's mechanical energy, we complete the system by designing and deploying a suitable power take-off system and analyze the new system's water-to-wire energy conversion performance.

ACKNOWLEDGEMENTS

MNMQ and FWZ would like to acknowledge the financial support from The Hong Kong Polytechnic University for their PhD studies. We would also like to thank Dr. Bingfu Zhang and Mr. Shu Wang for their kind help during this research.

REFERENCES

- Abiru H, Yoshitake A (2012) Experimental study on a cascade flapping wing hydroelectric power generator. *Journal of Energy and Power Engineering*, **6**: 1429-1436.
- Boudreau M, Dumas G, Rahimpour M, Oshkai P (2018) Experimental investigation of the energy extraction by a fully-passive flapping-foil hydrokinetic turbine prototype. *Journal of Fluids and Structures*, **82**: 446-472.
- Boudreau M, Gunther K, Dumas G (2019) Free-pitching flapping foil turbines with imposed sinusoidal heave. *Journal of Fluids and Structures*, **90**: 110-138.
- Boudreau M, Picard-Deland M, Dumas G (2020) A parametric study and optimization of the fully-passive flapping-foil turbine at high Reynolds number. *Renewable Energy*, **146**: 1958-1975.
- Bryant M, Gomez JC, Garcia E (2013) Reduced-order aerodynamic modeling of flapping wing energy harvesting at low Reynolds number. *AIAA Journal*, **51**(12): 2771-2782.

Duarte L, Dellinger N, Dellinger G, Ghenaim A, Terfous A (2019) Experimental investigation of the dynamic behaviour of a fully passive flapping foil hydrokinetic turbine. *Journal of Fluids and Structures*, **88**: 1-12.

Dumas G, Kinsey T (2006) Eulerian simulations of oscillating airfoils in power extraction regime. *Advances in Fluid Mechanics VI*, WIT: 245-254.

Dunmon JA, Stanton SC, Mann BP, Dowell EH (2011) Power extraction from aeroelastic limit cycle oscillations. *Journal of Fluids and Structures*, **27**: 1182-1198

Isogai K, Abiru H (2012) Study of multi-wing configuration of elastically supported flapping wing power generator. *Transactions of The Japan Society Aeronautical and Space Sciences*, **55**(2): 133-142.

Jiang W, Wang Y, Zhang D, Xie Y (2020) Numerical investigation into the energy extraction characteristics of 3D self-induced oscillating foil. *Renewable Energy*, **148**: 60-71.

Jones KD, Davids S, Platzer MF (1999) Oscillating-wing power generation. in *Proceedings of the 3rd ASME/JSME Joint Fluids Engineering Conference, San Francisco, California, USA, July 1999*.

Kinsey T, Dumas G (2008) Parametric study of an oscillating airfoil in a power extraction regime. *AIAA Journal*, **46**(6): 1318-1330.

Kinsey T, Dumas G (2012) Computational fluid dynamics analysis of a hydrokinetic turbine based on oscillating hydrofoils. *Journal of Fluids Engineering*, **134**(2): 16.

McKinney W, DeLaurier J (1981) The wingmill: An oscillating-wing windmill. *Journal of Energy*, **5**(2): 109.

Peng Z, Zhu Q (2009) Energy harvesting through flow-induced oscillations of a foil. *Physics of Fluids*, **21**(12): 123601-123609.

Picard-Deland M, Olivier M, Dumas G, Kinsey T (2019) Oscillating foil turbine operating at large heaving amplitudes. *AIAA Journal*, **57**(12): 5104-5113.

Platzer MF, Sarigul-Klijn N (2009) A novel approach to extract power from free-flowing water and high altitude jet streams. In *Proceedings of the ASME 2009 3rd International Conference on Energy Sustainability*, **1**: 493–499, San Francisco, California, USA, July 2009.

- Platzer MF, Bradley RA (2009) Oscillating-wing power generator with flow induced pitch-plunge phasing. US Patent Pub. No. US20090121490A1.
- Sane SP, Dickinson MH (2002) The aerodynamic effects of wing rotation and a revised quasi-steady model of flapping flight. *Journal of Experimental Biology*, **205**: 1087-1096.
- Shimizu E, Isogai K, Obayashi S (2008) Multi objective design study of a flapping wing power generator. *Journal of Fluids Engineering*, **130**(2): 021104.
- Sun W, Jo S, Seok J (2019) Development of the optimal bluff body for wind energy harvesting using the synergistic effect of coupled vortex induced vibration and galloping phenomena. *International Journal of Mechanical Sciences*, **156**: 435-445.
- Taylor GK, Nudds RL, Thomas ALR (2003) Flying and swimming animals cruise at a Strouhal number tuned for high power efficiency. *Nature*, **425**(6959): 707-711.
- Triantafyllou MS, Triantafyllou GS, Yue DKP (2000) Hydrodynamics of fishlike swimming. *Annual Review of Fluid Mechanics*, **32**(1): 33-53.
- Veilleux JC, Dumas G (2017) Numerical optimization of a fully passive flapping airfoil turbine. *Journal of Fluids and Structures*, **70**: 102-130.
- Willert CE, Gharib M (1991) Digital particle image velocimetry. *Experiments in Fluids*, **10**: 181-193.
- Xiao Q, Liao W, Yang S, Peng Y (2012) How motion trajectory affects energy extraction performance of a biomimic energy generator with an oscillating foil. *Renewable Energy*, **37**(1): 61-75.
- Xiao Q, Zhu Q (2014) A review on flow energy harvesters based on flapping foils. *Journal of Fluids and Structures*, **46**: 174-191.
- Xu GD, Xu WH, Dai J (2017) Numerical and experimental study of a flapping foil generator. *Applied Ocean Research*, **63**: 242-250.
- Young J, Ashraf MA, Lai JCS, Platzer MF (2013) Numerical simulation of fully passive flapping foil power generation. *AIAA Journal*, **51**(11): 2727-2739.
- Zhu Q (2011) Optimal frequency for flow energy harvesting of a flapping foil. *Journal of Fluid Mechanics*, **675**: 495-517.